Pixel-Oriented Adaptive Apodization for Plane-Wave Imaging Based on Recovery of the Complete Dataset

Qi You, *Graduate Student Member, IEEE*, Zhijie Dong, *Graduate Student Member, IEEE*, Matthew R. Lowerison, and Pengfei Song, *Senior Member, IEEE*

***Abstract*— In theory, coherent plane-wave compounding (CPWC) enables ultrafast ultrasound imaging while maintaining a high imaging quality that is comparable to conventional B-mode imaging based on focused beam transmissions. However, in practice, due to the imperfect synthetization of transmit focusing (e.g., heterogeneous speed of sound in tissue and limited range of steering angle), CPWC suffers from a variety of imaging artifacts resulting from side lobes, grating lobes, and axial lobes. This study focuses on addressing the issues of axial lobes for CPWC, which constitutes an important source of clutter that leads to the degradation of contrast ratio and contrast-to-noise ratio (CR and CNR) of CPWC. We first investigated the source of the axial lobes based on plane-wave propagation and the delay-and-sum (DAS) beamforming. We then proposed a new method that is based on pixel-oriented adaptive apodization (POAA) to eliminate the axial lobes throughout the entire field of view (FOV). POAA was first validated in a simulation study, followed by *in vitro* phantom experiments and an *in vivo* case study on a carotid artery from a healthy volunteer. In the simulation study, suppression of axial lobes by 120 dB was observed from wire targets, and an improvement of CNR by up to 60% was found in a cyst-mimicking digital phantom. In the phantom experiment, POAA showed an improvement in CNR by around 20% over conventional methods. The effectiveness of axial lobe suppression was finally demonstrated *in vivo*, where POAA showed a substantial suppression of clutters throughout the entire FOV.**

***Index Terms*— Apodization, beamforming, complete dataset, compounding plane-wave imaging, microvessel imaging, synthetic aperture imaging, ultrafast imaging.**

Manuscript received September 8, 2021; accepted October 29, 2021. Date of publication November 2, 2021; date of current version January 26, 2022. This work was supported by the National Cancer Institute and the National Institute of Biomedical Imaging and Bioengineering of the National Institutes of Health under Grant R00CA214523 and Grant R21EB030072. The content is solely the responsibility of the authors and does not necessarily represent the official views of the National Institutes of Health. *(Corresponding author: Pengfei Song.)*

This work involved human subjects or animals in its research. The authors confirm that all human/animal subject research procedures and protocols are exempt from review board approval.

Qi You is with the Department of Bioengineering, Beckman Institute for Advanced Science and Technology, University of Illinois at Urbana–Champaign, Urbana, IL 61820 USA.

Zhijie Dong and Matthew R. Lowerison are with the Department of Electrical and Computer Engineering, Beckman Institute for Advanced Science and Technology, University of Illinois at Urbana–Champaign, Urbana, IL 61820 USA.

Pengfei Song is with the Department of Bioengineering, Beckman Institute for Advanced Science and Technology, University of Illinois at Urbana–Champaign, Urbana, IL 61820 USA, and also with the Department of Electrical and Computer Engineering, Beckman Institute for Advanced Science and Technology, University of Illinois at Urbana–Champaign, Urbana, IL 61820 USA (e-mail: songp@illinois.edu).

Digital Object Identifier 10.1109/TUFFC.2021.3124821

I. Introduction

COHERENT plane-wave compounding (CPWC) is a powerful ultrasound imaging technique that provides a very high imaging frame rate of up to tens of thousands of frames per second [1]. Such a high frame rate has enabled many novel imaging methods, such as shear wave elastography [2], ultrafast microvessel imaging [3], [4], and super-resolution ultrasound localization microscopy [5]. It was demonstrated that multiple plane-wave transmissions tilted in different angles could achieve equivalent imaging quality as conventional focused beam transmissions based on the principle of transmit focusing synthetization [1]. However, the heterogeneous distribution of the speed of sound in tissue and the limited number of steering angles that are practically available (e.g., a high number of steering angles lead to a reduced imaging frame rate) undermine the transmit focus synthetization in CPWC, resulting in broadened main lobes and elevated side lobes and grating lobes that deteriorate imaging quality [6]–[10].

Another source of noise associated with CPWC is axial lobes, which produce artifacts that spread in the axial direction beyond the main lobe [11]. Different from side lobes and grating lobes in CPWC, axial lobes are not associated with transmit focus synthetization and cannot be suppressed by manipulating the steering angles [11]. As demonstrated in Fig. 1, while increasing the number of steering angles significantly reduces the grating lobe and sidelobe level for CPWC, the axial lobe is largely unaffected. An effective method that reduces the axial lobe is transmit apodization, which also suppresses side lobes at the cost of broadened main lobe [13]. Rodriguez-Molares *et al.* [11], [12] has shown that axial lobes can be suppressed in a limited field of view (FOV) by applying the angle-dependent transmit apodization (ADTA). ADTA functions by filtering out axial lobe clutters that are typically generated by transducer elements that are far away from the targeted pixel. One limitation of the conventional

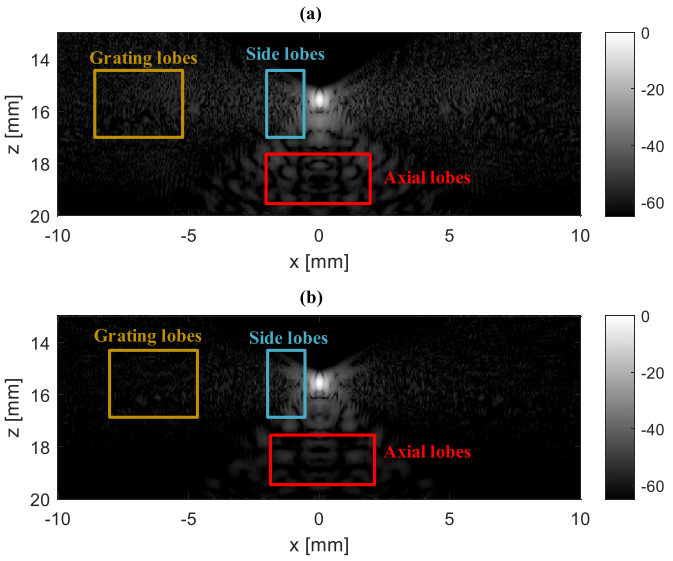

Fig. 1. Simulation images of a wire target (i.e., PSF) generated by CPWC with different numbers of steering angles. (a) Steering angles range from −15° to 15° with a step size of 3° (CPWC 11 angles' transmission). (b) Steering angles range from −15° to 15° with a step size of 1° (CPWC 31 angles' transmission).

ADTA method is that, as the transmit apodization profile varies spatially with the target location, ADTA can only be configured for a local region that is much smaller than the full FOV. As a result, the large area of the remaining FOV that is not subject to ADTA remains contaminated by clutters resulting from both axial and side lobes.

In order to address this limitation associated with conventional ADTA and enable ADTA throughout the entire FOV, here, we introduce a new method called pixel-oriented adaptive apodization (POAA), which incorporates the pixel location as a variable into the axial lobe analysis and apodization profile generation. The optimized transmit apodization in POAA correlates with both the transmit steering angle and the image geometry, which allows POAA to suppress the axial lobes to a negligible level throughout the entire FOV. In practice, since the transmit apodization is realized by applying different voltages to each transducer element, only one apodization profile can be realized in each pulse–echo cycle. Therefore, for the purpose of POAA, it is impossible to adjust transmit apodization and reemit for every imaging pixel.

To achieve POAA in practice, we propose to leverage the complete dataset that can be recovered from techniques, such as synthetic transmit aperture (STA) imaging [14]–[16]. In each pulse–echo cycle, STA transmits with a single element (or with a single virtual source that consists of multiple elements) and records the backscattered signal corresponding to the single transmit element. The process iterates until all the elements or virtual sources have been transmitted and recorded. The resulting complete dataset allows synthetization of arbitrary transmit sequences with arbitrary apodization [14], which is ideal for POAA. Since conventional STA suffers from a low signal-to-noise ratio (SNR), we implemented several encoding techniques to improve SNR, including the Hadamard spatial encoding and delay encoding [17]–[21], [25]. The Hadamard technique encodes the transmit signal amplitude for each transducer element with the Hadamard matrix, followed by decoding with the inverse Hadamard matrix. This allows simultaneous transmission of all the transducer elements for each pulse–echo cycle (i.e., N elements instead of just 1 as in conventional STA), which effectively boosts the SNR by $\sqrt{N}$ [17]. Similarly, the delay encoding technique encodes the transmit events by applying transmit time delays that are phase-encoded, whose inverse or pseudoinverse can be used for decoding purposes. Unlike the Hadamard encoding, the delay encoding technique does not involve inverting the polarity of the transmit pulses to achieve coding and decoding (e.g., the $+1$ and -1 pulses must be perfectly canceled in decoding when using Hadamard). Instead, the delay encoding only requires adjustment of the transmit delays as what is used in steering and focusing. Therefore, delay encoding may be more convenient and robust to implement in practice on ultrasound systems.

Although both Hadamard encoding and delay encoding can be employed to facilitate the realization of POAA, it is worth noting that, for an N-element ultrasound transducer, both Hadamard encoding and delay encoding expect N transmissions to completely recover the echo signal from each element. Although Bottenus and Nick [21], [25] have demonstrated that image reconstruction with fewer than N transmissions is feasible, the signal from an individual element may not be fully recovered by delay encoding with fewer than N transmissions, which is also true for the Hadamard encoding. Like conventional STA, the large number of transmit–receive events considerably limits the frame rate of POAA compared to CPWC. To balance the image quality enhancement and frame rate, we investigated the feasibility of reducing the number of transmissions (e.g., less than N) for the recovery of the complete dataset. We studied the relationship between the number of transmissions and imaging quality improvement to make POAA a more practical approach for different applications.

The rest of this article is organized as follows. In Section II, we first present the theory of axial lobe generation and the principles of POAA. Then, the experimental setup that includes simulation studies, phantom studies, and *in vivo* experiments on the carotid artery of a healthy volunteer is introduced. In Section III, the results of all the experiments are presented. In Sections IV and V, we finalize this article with discussion and conclusions.

II. Methods

A. Source of the Axial Lobes in CPWC

A typical configuration of CPWC is shown in Fig. 2(a). A linear array transducer consisting of N elements transmits ultrasound pulses toward the target medium. In an ideal coherent plane-wave transmission, every element emits a pulsed spherical wave with a time delay that is indicated by the steering angle α_T in the Tth transmission. For example, for the nth element located at $(x_n, 0)$, the transmit delay is given by $\tau_n = x_n * \sin(\alpha_T)/c$, where c is the reference speed of sound in the medium [1].

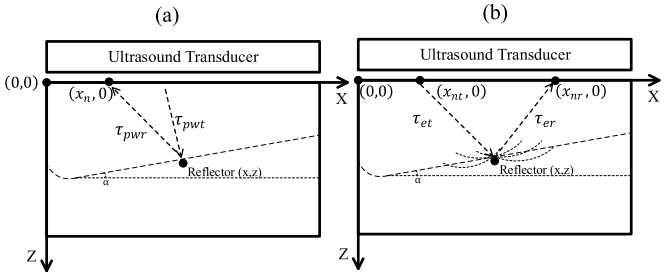

Fig. 2. (a) Schematic of a single plane-wave incident on a single reflector with a steering angle of α. The TOF from the transducer to the reflector is τ_{pwt}. The TOF from the reflector to an arbitrary element is τ_{pwr}. (b) TOF of multiple spherical waves. The transmission time from every element to the reflector is τ_{et}. The transmission time from the reflector to every element is τ_{er}.

For delay-and-sum (DAS) beamforming, the transmit and receive times of flight (TOF) are essential for calculating the correct time delays for coherent summation of the recorded ultrasound signal. As shown in Fig. 2(a), the transmit TOF τ_{pwt} from the transducer to a reflector at (x, z) is given by

$$\tau_{\text{pwt}}(T) = \frac{z\cos(\alpha_T) + x\sin(\alpha_T)}{c}. \tag{1}$$

The receive TOF from the reflector to the nth element at $(x_n, 0)$ is given by

$$\tau_{\text{pwr}}(n) = \frac{\sqrt{z^2 + (x - x_n)^2}}{c}. \tag{2}$$

With an ultrasound transducer with N elements, and assuming that the received echo signal is a time-delayed version of the transmit signal, we can write the echo signal from point (x, z) as

$$S_{\text{expect}}(x, z) = \sum_{T=1}^{M}\sum_{n=1}^{N} h\big(t - \tau_{\text{pwt}}(T) - \tau_{\text{pwr}}(n)\big) \tag{3}$$

where $S_{\text{expect}}(x, z)$ represents the expected receive signal of CPWC from reflector located at (x, z), M denotes the total number of transmissions with different steering angles, and h represents the transmitted signal in every transmission.

For a fixed point (x, z), delay τ_{pwt} is a function of steering angle α_T in the Tth transmission and delay τ_{pwr} is a function of x_n indicating the position of the nth element. The inner summation means the superposition of the receive signals from all the elements. The outer summation means the superposition of the reflected signals from all the transmissions.

However, if we analyze the wave propagation from each element as a spherical wave instead of a plane wave emitted from the entire array, we can calculate the TOF of the spherical wave between each transducer element and the target. As shown in Fig. 2(b), the TOF from the transmit element at $(x_{nt}, 0)$ to the reflector (x, z) is

$$\tau_{\text{et}}(n, T) = \frac{x_{nt}\sin(\alpha_T) + \sqrt{z^2 + (x - x_{nt})^2}}{c}. \tag{4}$$

The TOF from the reflector (x, z) to element located at $(x_{nt}, 0)$ is

$$\tau_{\text{er}}(n) = \frac{\sqrt{z^2 + (x - x_{nr})^2}}{c}. \tag{5}$$

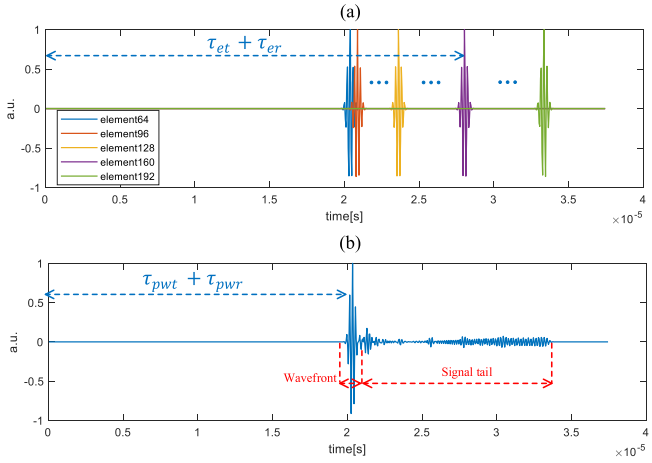

Fig. 3. (a) Plot of received RF signals from transmitting every single element (individual signals). (b) Plot of the received RF signal from transmitting a plane wave with all the transducer elements (CPWC signal). The signal in (b) is essentially the linear superposition of signals recorded in (a). The TOF of the main pulse from the element that is closest to the target location is $\tau_{\text{pwt}} + \tau_{\text{pwr}}$. Following the main pulse is the signal tail whose length depends on the temporal range of the spherical wave from each element (i.e., $\tau_{\text{et}} + \tau_{\text{er}}$).

By superposition, the CPWC signal from this time measurement is given by

$$S_{\text{real}}(x, z) = \sum_{T=1}^{M}\sum_{n=1}^{N} h(t - \tau_{\text{et}}(n, T) - \tau_{\text{er}}(n)) \tag{6}$$

where $S_{\text{real}}(x, z)$ represents the actual receive signal of CPWC from the reflector point (x, z).

For the two TOF calculations in (3) and (6), the receive TOF τ_{pwr} in (2) is identical to the receive TOF τ_{er} in (5). However, the transmit TOF τ_{et} in (4) can be different from the transmit TOF τ_{pwt} in (1). For CPWC, it is assumed that all the transmit signals (i.e., the plane wave) from each element arrive at the target location at the same time, $t = \tau_{\text{pwt}}$. In reality, spherical waves from individual elements arrive at the location at different times [see Fig. 2(b)]. The TOF for the element that is closest to the target (i.e., right on top of the target) has approximately the same transmit TOF between the plane wave and the spherical wave scenario. For the rest of the elements that are further away from the target location, τ_{et} no longer matches τ_{pwt}. The spherical waves that arrive later at the target location will form a long "tail" behind the incident plane wave, which manifests in the form of axial lobes upon beamforming. This is further illustrated in the simulated waveforms in Fig. 3 where one can see that the plane wave only has a matched transmit and receive TOF with the TOF recorded from element 64 (the element that is closest to the target). The superposition of the remaining pulses from the rest of the transducer elements results in a long tail trailing the wavefront. During DAS, the tail will generate artifacts (i.e., the axial lobes) beyond the depth of the main lobe. The length of the extent of the axial lobe depends on the maximum distance from the transmit element to the target point.

B. Principles of POAA

According to the analysis above, axial lobes are generated from spherical waves that arrive at the target location at a much later time than the wavefront of the incident plane wave. Therefore, to eliminate the axial lobe, one needs to remove the late-arrival spherical waves by suppressing the transmission of the corresponding transducer elements. Rodriguez-Molares *et al.* [11] provided a solution to determine which transducer elements need to be suppressed (i.e., apodization). The discrepancy in transmit TOF between each spherical wave and the incident plane wave can be estimated and compared against a predefined threshold

$$\left|\tau_{\text{pwt}} - \tau_{\text{et}}\right| < \varepsilon \tag{7}$$

where ε is the error threshold to limit the transmit TOF difference between the plane wavefront and the spherical wave from each transducer element. Equation (7) can be rewritten by using (1) and (4), which becomes

$$\left|z\cos(\alpha) + x\sin(\alpha) - x_{nt}\sin(\alpha) - \sqrt{z^2 + (x - x_{nt})^2}\right| < \varepsilon c. \tag{8}$$

If we assume $\tau_{\text{et}} > \tau_{\text{pwt}}$, or the part within the absolute value function in the left-hand side of (8) is negative, and then, define $L = \varepsilon c + z\cos(\alpha) + x\sin(\alpha)$, (8) can be rewritten as

$$\sqrt{z^2 + (x - x_{nt})^2} < L - x_{nt}\sin(\alpha). \tag{9}$$

After squaring both sides, we get

$$z^2 + x^2 - 2xx_{nt} + x_{nt}^2 < L^2 + x_{nt}^2\sin^2(\alpha) - 2Lx_{nt}\sin(\alpha). \tag{10}$$

Equation (10) can be rearranged as

$$x_{nt}^2\cos^2\alpha + 2x_{nt}(L\sin\alpha - x) + z^2 + x^2 - L^2 < 0. \tag{11}$$

If we assume $\tau_{\text{et}} \leq \tau_{\text{pwt}}$, or the part within the absolute value function in the left-hand side of (8) is positive, and define $L = z\cos(\alpha) + x\sin(\alpha) - \varepsilon c$, then repeating a similar procedure from (9) to (11) will get the same result as in (11). Equation (11) is a quadratic equation and has the solution of

$$\frac{x - L\sin\alpha - \sqrt{\Delta}}{\cos^2\alpha} < x_{nt} < \frac{x - L\sin\alpha + \sqrt{\Delta}}{\cos^2\alpha}, \quad \Delta > 0$$
$$\text{where } \Delta = x^2\sin^2\alpha - z^2\cos^2\alpha + L^2 - 2Lx\sin\alpha \tag{12}$$

where x_{nt} represents the x coordinate of the transmit element. Define $x_{nt} = (n_{\text{active}} - 1/2) * P$, where n_{active} is the index of the activated elements in the apodization. P represents the pitch size. Equation (12) can be further expressed with element index n_{active} as a variable

$$\frac{x - L\sin\alpha - \sqrt{\Delta}}{P\cos^2\alpha} + \frac{1}{2} < n_{\text{active}} < \frac{x - L\sin\alpha + \sqrt{\Delta}}{P\cos^2\alpha} + \frac{1}{2}. \tag{13}$$

Equation (13) denotes the range of the elements within the apodization profile that is activated, whereas the elements outside the range contribute to the axial lobes and are suppressed. To avoid Gibbs ringing and suppress side lobes, a Hanning window is further applied to the apodization. The final apodization function can be expressed as

$$\begin{aligned} w(n, x, z) &= 0.5\left(1 - \cos\left(2\pi\frac{n_i}{n_{\text{tot}}}\right)\right) \\ \text{where } n_i &= \left[n_{\text{active}} - \frac{x - L\sin\alpha - \sqrt{\Delta}}{P\cos^2\alpha} - \frac{1}{2}\right] \\ n_{\text{tot}} &= \left[\left(\frac{x - L\sin\alpha + \sqrt{\Delta}}{P\cos^2\alpha} + \frac{1}{2}\right)\right. \\ &\quad \left. - \left(\frac{x - L\sin\alpha - \sqrt{\Delta}}{P\cos^2\alpha} + \frac{1}{2}\right)\right] \\ &= \left[\frac{2\sqrt{\Delta}}{P\cos^2\alpha}\right] \end{aligned} \tag{14}$$

where $[\cdot]$ is the rounding operation. The length of the Hanning window n_{tot} is derived from the range of n_{active} in (13). The index of the Hanning window $n_i = 0, 1, 2, \ldots, n_{\text{tot}}$ equals to the index of the activated element n_{active} minus the index of the starting element. The final beamformed signal $S_{\text{POAA}}(x, z)$ with POAA can be expressed as

$$S_{\text{POAA}}(x, z) = \sum_{T=1}^{M}\sum_{n=1}^{N} w(n, x, z)h\big(t - \tau_{\text{pwt}}(T) - \tau_{\text{pwr}}(n)\big). \tag{15}$$

As indicated in (13) and (14), the apodization is a function of both steering angle α and pixel location (x, z), which suggests that, for every transmission with a certain steering angle, every pixel has a different apodization that minimizes the discrepancy in transmit TOF between the plane wavefront and the spherical wave from each transducer element (hence, the minimal axial lobe). Therefore, in order to achieve axial lobe suppression throughout the entire FOV, one needs to transmit with pixel-location-dependent apodization: for example, if an FOV has 100 × 100 pixels, then one needs to transmit 100 × 100 = 10 000 times for each pixel location with the apodization that minimizes the axial lobe for that location. This is extremely challenging to carry out in practice. Although since the element index has to be integer and pixels that are spatially adjacent may share the same apodization, the number of transmissions needed is still on the order of several hundred to several thousand, which is practically prohibitive for real-time imaging.

C. Recovery of the Complete Dataset

To overcome the hurdle of a high number of transmissions for POAA, in this article, we propose to leverage the recovery of the complete dataset by using the principles of synthetic aperture imaging [14]. Since the complete dataset allows the synthetization of arbitrary transmit with arbitrary apodization, one can potentially realize POAA with much fewer number of transmissions (e.g., 128 transmissions for a transducer with 192 elements).

Concerning the issues of low SNR for conventional STA with a single element or a subgroup of elements [17], in this article, we use both Hadamard encoding and delay encoding to acquire the complete dataset for every transducer element. The Hadamard encoding has been described by many other papers [17]–[19]. Therefore, we only briefly review the principles of the Hadamard encoding here in order to describe the decoding theory with incomplete transmissions that will be introduced later.

Denoting $\boldsymbol{M}_t$ as the transmit signal matrix of every single element, the Hadamard encoding can be expressed by the following equation:

$$\boldsymbol{M}_{t\_H} = \mathbf{H}\boldsymbol{M}_t \tag{16}$$

where $\boldsymbol{M}_{t\_H}$ is the Hadamard-encoded transmission. Based on superposition, the receive signal is also encoded with matrix $\mathbf{H}$

$$\boldsymbol{M}_{r\_H} = \mathbf{H}\boldsymbol{M}_r \tag{17}$$

where $\boldsymbol{M}_r$ is the receive signal of every transducer element and $\boldsymbol{M}_{r\_H}$ is the receive signal after the Hadamard encoding. In conventional Hadamard encoding, the Hadamard matrix $\mathbf{H}$ is an $N \times N$ matrix composed of only 1s and -1s, which means that, for a transducer with N elements, a total number of N transmissions is required to fully encode and decode the matrix. For every transmission, the receive signal $\boldsymbol{M}_{r\_H}$ is encoded with the nth row of the Hadamard matrix. Thus, $\boldsymbol{M}_{r\_H}$ is a column vector with the same size as $\boldsymbol{M}_r$. The decoding process then simply becomes

$$\boldsymbol{M}_r = \mathbf{H}^{-1}\boldsymbol{M}_{r\_H}. \tag{18}$$

Since the Hadamard matrix $\mathbf{H}$ is orthogonal and symmetric, its inverse and transpose are identical: $\mathbf{H}^{-1} = \mathbf{H}^T$.

In practice, a total number of N transmissions (e.g., 128 for a 128-element transducer) may be too high or expensive for real-time imaging. Therefore, we also investigated the case of using a smaller number of transmissions (e.g., less than N) for complete data recovery. For example, we can use an $M \times N$ matrix to encode the transmit signal, where M is the number of transmissions and is less than N. The encoding procedure remains the same except for $\boldsymbol{M}_{r\_H}$, which becomes a column vector of length M. For the decoding process, since $\mathbf{H}$ is no longer invertible, we use pseudoinverse and regularization methods [24], which are given by

$$\boldsymbol{M}_r = \min_{\boldsymbol{M}_r} \left\| \boldsymbol{M}_{r\_H} - \mathbf{H}\boldsymbol{M}_r \right\|^2 + \beta \|\boldsymbol{M}_r\|^2 \tag{19}$$

where β is the coefficient of the L2 regularization. The solution of (19) is given by [24]

$$\boldsymbol{M}_r = \left(\mathbf{H}^T\mathbf{H} + \beta\mathbf{I}\right)^{-1}\mathbf{H}^T\boldsymbol{M}_{r\_H} \tag{20}$$

where $\mathbf{I}$ is the identity matrix.

Besides the Hadamard encoding, we also applied the delay encoding technique to recover the individual channel data from the receive signal [20], [21]. Since delay encoding does not involve inverting the polarity of the transmit pulses, it can be more robust for decoding since the Hadamard encoding technique requires the positive and negative pulses to exactly cancel out for robust decoding. In delay encoding, every transmit channel uses the transmit signal of the same amplitude but different time delays. Denoting the original transmit signal of the nth channel as $m_n(t)$, the transmit signal after delay encoding becomes $m_n(t - \Delta t_n)$. Here, Δt_n represents the time delay added to the nth transmit channel. According to the delay property of the Fourier transform, applying a delay in the time domain is equivalent to applying a phase shift in the Fourier domain. Therefore, the Fourier transform of $m_n(t - \Delta t_n)$ is

$$\mathcal{F}[m_n(t - \Delta t_n)] = e^{-j2\pi f \Delta t_n}\mathcal{F}[m_n(t)] \tag{21}$$

where $\mathcal{F}[\cdot]$ denotes the Fourier transform operation and f represents the frequency variable in the Fourier domain.

Assuming that we have M transmissions with N elements encoded by different time delays, the delay matrix $\mathbf{D}$ is an $M \times N$ matrix with every element d_{xy} expressed as

$$d_{ab} = \Delta t_{ab}, \quad a = 1, 2, 3, \ldots, M, \ b = 1, 2, 3, \ldots, N \tag{22}$$

where Δt_{ab} is the time delay applied to the bth transmit element in the ath transmission. Similarly, we can construct the delay matrix $\mathbf{H}_d$ in the Fourier domain with every entry $h_{d_{ab}}$ as

$$h_{d_{ab}} = e^{-j2\pi f d_{ab}}. \tag{23}$$

Thus, the delay encoding process can be expressed as

$$\mathcal{F}\left[\boldsymbol{M}_{t\_D}\right] = \mathbf{H}_d\mathcal{F}[\boldsymbol{M}_t] \tag{24}$$

$$\mathcal{F}\left[\boldsymbol{M}_{r\_D}\right] = \mathbf{H}_d\mathcal{F}[\boldsymbol{M}_r]. \tag{25}$$

Similar to (16) and (17), M_t and M_r represent the transmit and receive signals of every single element. $\boldsymbol{M}_{t\_D}$ and $\boldsymbol{M}_{r\_D}$ represent the transmit and receive signals of every transmission after delay encoding.

In (22)–(25), Δt_{ab} should be selected to make $\mathbf{H}_d$ have higher rank so that the decoding process can be more robust. Gong *et al.* [20] used a binary state delay matrix, which only includes zero delay and half period delay. The delay matrix was designed following the construction of the Hadamard matrix where zero delay represents 1s and half period delay represents 0s. However, for incomplete transmissions (i.e., $M < N$), the number of transmission M is smaller than the number of elements, so $\mathbf{H}_d$ cannot be constructed as a Hadamard matrix. In this article, we propose to use a random delay-based method to construct the delay matrix. The procedure of constructing $\mathbf{H}_d$ is described as follows.

1) *Step 1:* Generate an $M \times N$ random number matrix as the delay matrix $\mathbf{D}$ whose elements are within the interval $(0, d_{\max})$, where $d_{\max}$ represents the maximum delay applied in the transmissions. The selection of $d_{\max}$ does not affect the performance of delay encoding. In this article, $d_{\max}$ was set at 2.4 μs.
2) *Step 2:* Calculate $\mathbf{H}_d$ and its rank for every sampled frequency f, as denoted in (23).
3) *Step 3:* If the rank of $\mathbf{H}_d$ for every frequency f (except $f = 0$) equals to $\min(M, N)$, the random delay matrix $\mathbf{D}$ is considered optimal; otherwise, regenerate a new matrix $\mathbf{D}$ by repeating steps 1 and 2.

Typically, one or two trials will generate the appropriate random delay matrix $\mathbf{D}$ and encoding matrix $\mathbf{H}_d$. Then, we can encode the transmit and receive signals, as denoted in (24) and (25).

The delay decoding process is analogous to the Hadamard decoding except that the signal needs to be transformed to the Fourier domain first. The pseudoinversion of (25) is

$$\mathcal{F}[\boldsymbol{M}_r] = \left(\mathbf{H}_d^T\mathbf{H}_d + \beta\mathbf{I}\right)^{-1}\mathbf{H}_d^T\mathcal{F}\left[\boldsymbol{M}_{r\_D}\right]. \tag{26}$$

Similar to (19) and (20), β is the coefficient of the L2 regularization in the inverse problem of the following equation:

$$\mathcal{F}[\boldsymbol{M}_r] = \max_{\mathcal{F}[\boldsymbol{M}_r]} \left\|\mathcal{F}\left[\boldsymbol{M}_{r\_D}\right] - \mathbf{H}_d\mathcal{F}[\boldsymbol{M}_r]\right\|^2 + \beta\|\mathcal{F}[\boldsymbol{M}_r]\|^2. \tag{27}$$

D. Simulation Study

A simulation study based on Field II [22], [23] was first designed to test the performance of the newly proposed POAA method. Point targets and a 3.5-mm-diameter anechoic cyst at 15.5-mm depth were both simulated. The simulation was based on a 192-element, 230-μm-pitch linear array transducer with a center frequency of 5.2 MHz and 60% bandwidth. For the point target simulation, 31 compounding angles from $-15°$ to $15°$ with a $1°$ step size were used for both CPWC, ADTA, and POAA. The lateral and axial profiles across the single-point target were measured as quantification of lateral and axial resolutions, respectively. The lateral profile was also used to measure the grating lobe and sidelobe levels, while the axial profile was used to quantify the axial lobe level.

For the digital cyst simulation, we applied CPWC and POAA with different numbers of transmissions with different steering angles. The steering angle ranges from $-15°$ to $15°$ with a step size of $30°/N_{\text{trans}}$. Here, N_{trans} is the number of compounding angles used in transmissions and was set to integer multiples of 8 (e.g., 8, 16, 32, ..., 192). Both the contrast-to-noise ratio (CNR) and the contrast ratio (CR) were calculated to compare imaging performance. CNR and CR are given by

$$\text{CNR} = \frac{|u_i - u_o|}{\sqrt{\sigma_i^2 + \sigma_o^2}} \tag{28}$$

$$\text{CR} = \frac{u_i}{u_o} \tag{29}$$

where u_i and u_o denote the mean pixel intensity inside and outside the cyst, respectively; and σ_i^2 and σ_o^2 represent the variance of pixel intensity inside and outside the cyst, respectively. These four variables can be expressed as

$$u_i = E\{p_i\}, \quad u_o = E\{p_o\} \tag{30}$$

$$\sigma_i^2 = E\left\{(p_i - u_i)^2\right\}, \quad \sigma_o^2 = E\left\{(p_o - u_o)^2\right\} \tag{31}$$

where $E\{\cdot\}$ represents the expectation, and p_i and p_o denote the pixel intensity values inside and outside the cyst separately.

TABLE I
SPECIFICATION OF VERASONICS DATA ACQUISITION

Parameter	Value	Unit
Array Geometry	Linear	-
Number of Elements	192	elements
Element Pitch	230	μm
Element Width	207	μm
Center Frequency	5.2	MHz
Elevation Focus	20	mm
Fractional Bandwidth	60%	-
Steering Angles	[-15,15]	degree

E. In Vitro and in Vivo Experiment in Vitro

phantom experiment and *in vivo* experiment were both conducted using a Verasonics Vantage 256 System (Verasonics, Kirkland, WA, USA). A 192-element, 230-μm-pitch linear array transducer 9L-D (GE Healthcare, Wauwatosa, WI, USA) was used to transmit at a 5.2-MHz center frequency. The specifications of the *in vitro* and *in vivo* data acquisition sequence are listed in Table I.

For the *in vitro* phantom experiment, a commercial ultrasound imaging phantom manufactured by CIRS (Model 040GSE, Norfolk, VA) was used to scan the anechoic cyst target (3-mm diameter) located at 15-mm depth. Both the Hadamard encoding and delay encoding were used to recover the complete dataset. We used both complete transmissions ($N = 192$) and incomplete transmissions to perform the encoding and decoding processes. Seven different transmission numbers ranging from 8 to 192 were used. The recovered complete dataset was then used to perform POAA. For every transmission number, CPWC and STA imaging were conducted correspondingly to provide a benchmark for POAA. Steering angles ranging from $-15°$ to $15°$ with a step size of $1°$ were used for POAA. Similar to the simulation study, both CNR and CR were measured to evaluate the imaging performance of POAA.

For *in vivo* experiment, the carotid artery of a healthy volunteer was scanned to collect data for CPWC imaging. Similar to the *in vitro* study, the Hadamard encoding and delay encoding with both complete ($N = 192$) and incomplete transmissions ($N = 32$, 96, 128, and 192) were performed to recover the complete dataset and synthesize ADTA and POAA signals. CPWC and STA imaging were also performed to provide a benchmark for comparison with POAA. All four types of transmission were programmed in the same acquisition sequence such that motion from the carotid artery was minimal. Clutter level inside the vessel lumen was measured to quantify the suppression of axial lobes by POAA.

III. RESULTS

Fig. 4 shows the comparison between conventional CPWC, CPWC with ADTA [11], and the proposed POAA. All the results were from simulations of three point targets located at 15.5-mm depth separated by 5 mm in the lateral direction. In Fig. 4(a), the conventional CPWC image has considerable axial lobes and side lobes around all the three point targets.

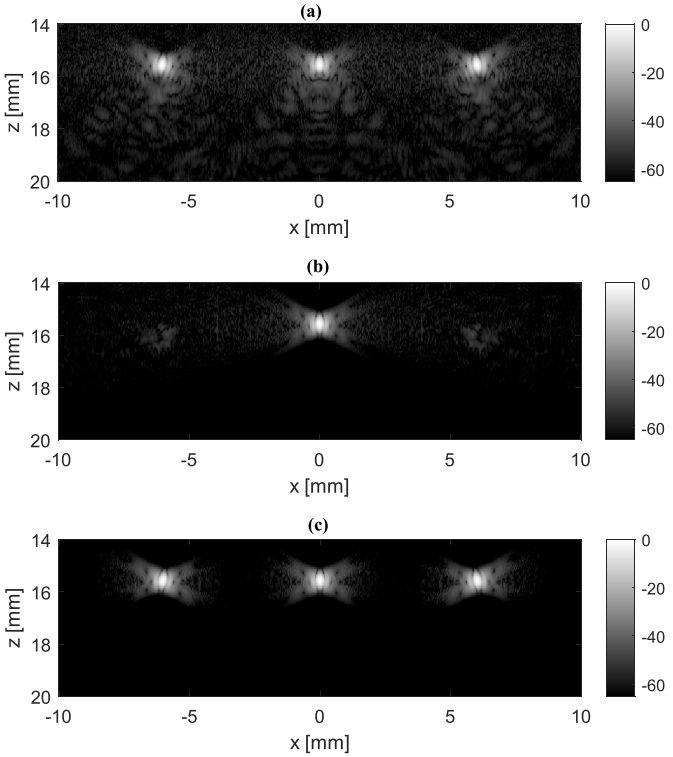

Fig. 4. Simulation of three point targets using (a) conventional CPWC, (b) CPWC with ADTA, and (c) CPWC with POAA. POAA demonstrated improved imaging quality throughout the entire FOV, while ADTA is only effective for the central region of the image. All images are displayed using a 65-dB dynamic range.

In Fig. 4(b), ADTA was configured for the point target in the middle. As a result, only the point target in the middle showed improved imaging quality, however, at the cost of deteriorated imaging quality for off-center targets. In contrast, as shown in Fig. 4(c), it can be clearly seen that POAA was capable of improving the imaging quality for all the three point targets across the entire FOV.

To characterize the point spread function (PSF) of POAA, a single-point target was simulated and imaged by CPWC alone [see Fig. 5(a)] and CPWC combined with POAA [see Fig. 5(b)]. CPWC used 31 compounding angles. As shown in the quantitative measurements in Fig. 5(b) and (c), POAA reduced the axial lobe level by approximately 120 dB at 2 mm beyond the peak of the main lobe. The marked improvement can be clearly visualized from the B-mode images shown in Fig. 5(a) and (b). In addition, POAA also reduced the side and grating lobe level by approximately 20 dB on average, as shown in Fig. 5(c).

Fig. 6 shows the reconstructed images of the simulated anechoic cyst using different beamforming methods. The clutters induced by the axial and side lobes can be clearly visualized from the cyst region constructed by CPWC [see Fig. 6(a)–(c)]. In contrast, under the same number of compounding angles, POAA effectively reduced the clutter level inside the anechoic cyst region due to effective suppression of both axial and side lobes. This can be further demonstrated by the quantitative measurements using CNR and CR, as shown in Fig. 7. The CNR and CR were calculated using (28)–(31). As shown

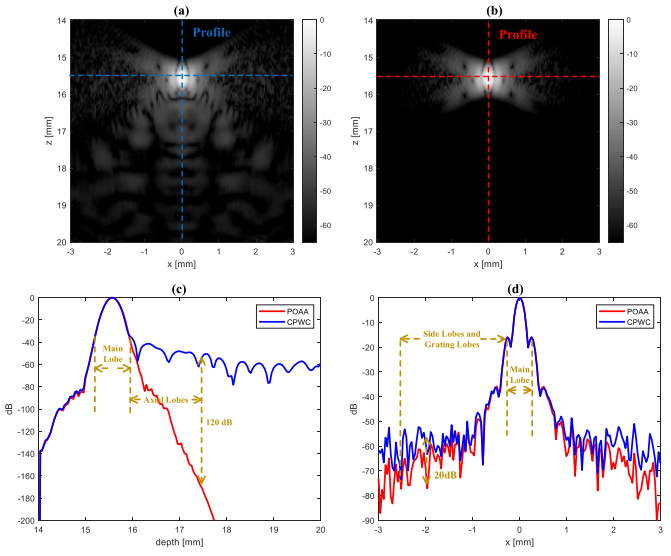

Fig. 5. (a) and (b) Simulated point target imaged by CPWC with POAA and without POAA [(a) CPWC PSF and (b) POAA PSF]. (c) Axial profile across the reflector. (d) Lateral profile across the reflector. All images are displayed using a 65-dB dynamic range.

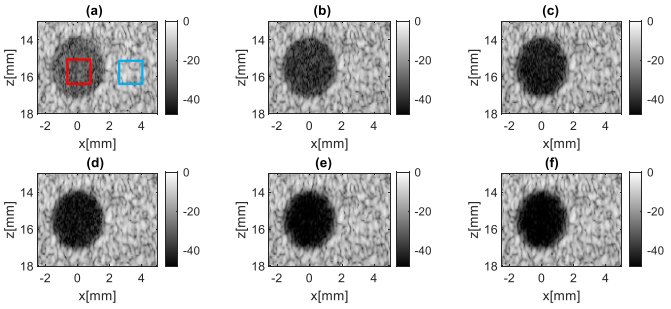

Fig. 6. Simulated anechoic cyst of CPWC with POAA and without POAA by different numbers of steering angles. (a) and (d) Eight transmission angles. (b) and (e) 32 transmission angles. (c) and (f) 192 transmission angles. All images are displayed using a 50-dB dynamic range. The red and blue rectangles in (a) denote the ROI used for measuring the CNR and CR. The red rectangle encloses the region inside the cyst, while the blue rectangle encloses the region outside the cyst. (a) CPWC eight angles. (b) CPWC 32 angles. (c) CPWC 192 angles. (d) POAA eight angles. (e) POAA 32 angles. (f) POAA 192 angles.

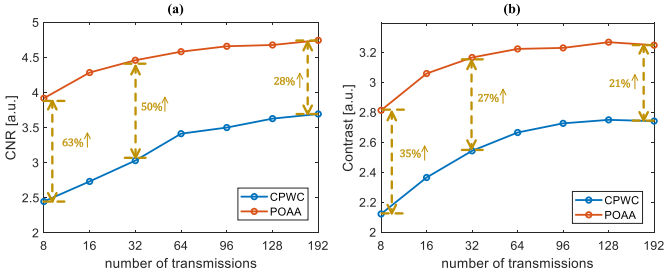

Fig. 7. (a) CNR and (b) CR measurements of the simulated cyst with a different number of transmission angles.

in Fig. 6(a), the region enclosed by the red square denotes the pixels inside the cyst, while the region enclosed by the blue square denotes the pixels outside the cyst. Increasing the number of compounding angles does alleviate the clutters resulting from the side lobes and grating lobes for CPWC but not for clutters resulting from axial lobes. On the other

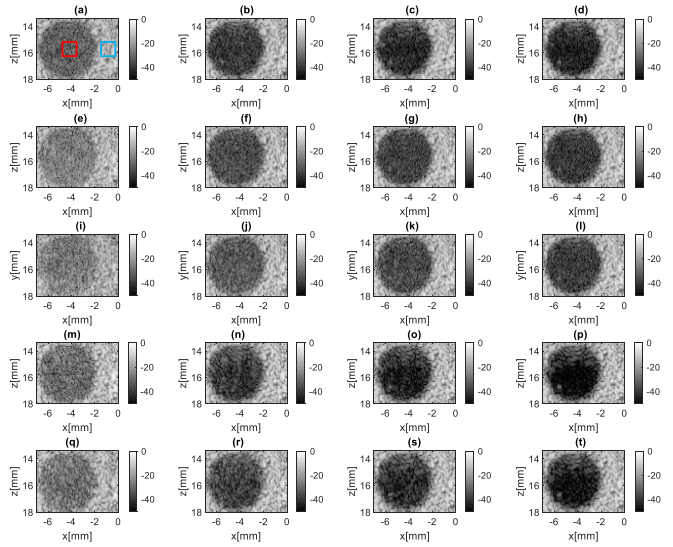

Fig. 8. *In vitro* cyst of CPWC (a)–(d) without POAA, (m)–(p) with POAA using Hadamard encoding (HD-POAA), (q)–(t) with POAA using delay encoding (DE-POAA) by a different number of steering angles, (e)–(h) synthetic aperture imaging using Hadamard encoding (HD-SA), and (i)–(l) synthetic aperture imaging using delay encoding (DE-SA). All images are displayed using a 50-dB dynamic range. The red and blue rectangles in (a) denote the ROI used for measuring the CNR and CR. The red rectangle encloses the region inside the cyst, while the blue rectangle encloses the region outside the cyst. (a) CPWC eight transmissions. (b) CPWC 64 transmissions. (c) CPWC 128 transmissions. (d) CPWC 192 transmissions. (e) HD-SA eight transmissions. (f) HD-SA 64 transmissions. (g) HD-SA 128 transmissions. (h) HD-SA 192 transmissions. (i) DE-SA eight transmissions. (j) DE-SA 64 transmissions. (k) DE-SA 128 transmissions. (l) DE-SA 192 transmissions. (m) HD-POAA eight transmissions. (n) HD-POAA 64 transmissions. (o) HD-POAA 128 transmissions. (p) HD-POAA 192 transmissions. (q) DE-POAA eight transmissions. (r) DE-POAA 64 transmissions. (s) DE-POAA 128 transmissions. (t) DE-POAA 192 transmissions.

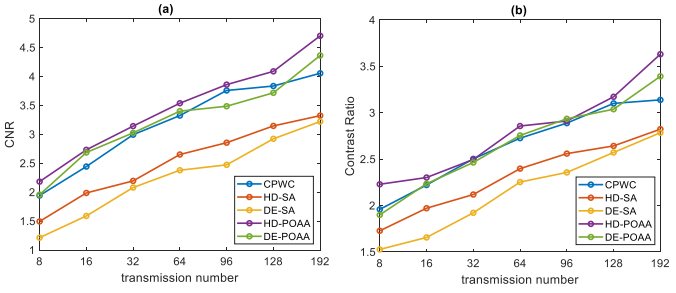

Fig. 9. (a) CNR and (b) CR curve of the *in vitro* cyst with different numbers of transmissions.

hand, POAA showed an improvement of 63% in CNR and 35% in CR over CPWC in the case of 8 compounding angles. Although the gap narrows with an increased number of compounding angles, POAA still demonstrated a CNR increase of 28% and a CR increase of 21% at the maximum number (192) of compounding angles.

Fig. 8 shows the *in vitro* phantom study results of an anechoic cyst from the CIRS phantom using the Verasonics Vantage system. Fig. 9 shows the associated quantitative CNR and CR measurements for the images in Fig. 8. The ROI shown in Fig. 8(a) is defined by the same method, as shown in Fig. 6(a). The CNR and CR curves shown in Fig. 9 indicate that POAA with the Hadamard encoding provides the greatest

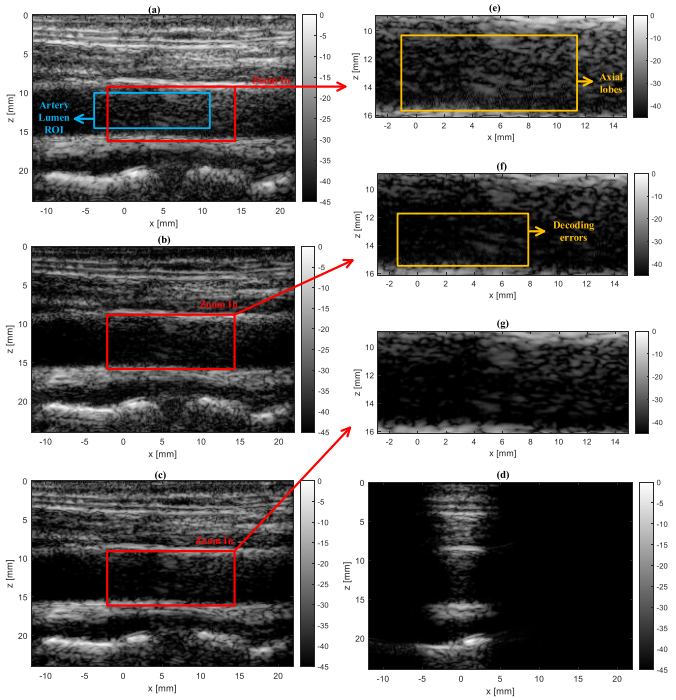

Fig. 10. CPWC and HD-SA images of a carotid artery using complete transmission ($N = 192$): (a) without POAA, (b) HD-SA imaging, (c) with POAA, (d) with ADTA, and (e)–(g) zoomed-in views of the local region enclosed by the red rectangle [(e) magnified local region for CPWC without POAA, (f) magnified local region for HD-SA, and (g) magnified local region for CPWC with POAA]. The region enclosed by the blue rectangle represents the ROI to measure the clutter level. The complete dataset used for SA and POAA was recovered by Hadamard encoding. All images are displayed using a 45-dB dynamic range.

improvement compared with other methods. From Fig. 8, it can be seen that, with eight transmissions, clutter in the anechoic region can be mostly attributed to electrical noise resulting from the low SNR and decoding error because of the low number of encoded transmissions. When the transmission number increases to 128, the axial lobes begin to show in the cyst, and POAA with the Hadamard encoding has around a 10% increase in CNR compared with CPWC. With 192 transmissions, both Hadamard encoding and delay encoding could generate signals with a minimal decoding error. Therefore, POAA using both Hadamard decoding and delay decoding has the optimal performance. As shown in Fig. 9, POAA demonstrated about a 20% increase in CNR and CR over CPWC.

Fig. 10 shows the *in vivo* images of the carotid artery using complete transmissions ($N_{\text{trans}} = 192$). In Fig. 10(a), the conventional CPWC image shows significant clutters inside the vessel lumen that deteriorates the image contrast. In Fig. 10(b), POAA provides clear clutter reduction in the entire FOV [e.g., yellow ROI in Fig. 10(d)]. On the contrary, as shown in Fig. 10(d), ADTA only works for the central region of the image. To measure the clutter level of Fig. 10(a) and (b), we mark the region from 11 to 15 mm in the axial direction and -5 to 10 mm in the lateral direction as the ROI [the region enclosed by the blue rectangle in Fig. 10(a)]. The average pixel intensity of the ROI is -40 dB in Fig. 10(a) and -47 dB in Fig. 10(b), which indicates that the contrast

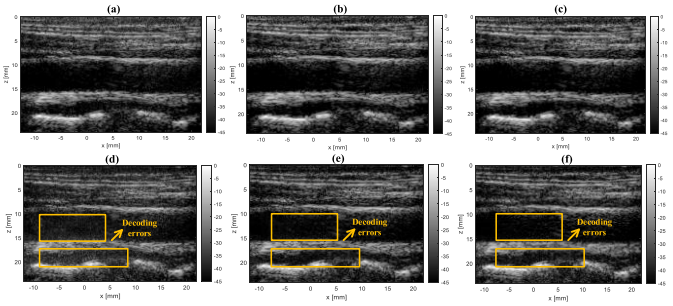

Fig. 11. CPWC (with POAA) and HD-SA images of a carotid artery using incomplete transmission: (a) and (d) $N = 32$, (b) and (e) $N = 96$, and (c) and (f) $N = 128$, respectively. The complete dataset used for SA and POAA was recovered by the Hadamard encoding. All images are displayed using a 45-dB dynamic range.

of the artery lumen is increased after suppressing axial lobes. In addition, Hadamard-encoded SA shows more artifacts in the deeper lumen region [see Fig. 10(c) and (f)], which can be a result of decoding errors. In comparison, CPWC with POAA in Fig. 10(g) is able to maintain the clutter rejection and showed minimal artifacts inside the vessel.

Fig. 11 shows the *in vivo* images of a carotid artery using an incomplete number of transmissions ($N_{\text{trans}} = 32/96/128$). Similarly, we measured the average pixel intensity of the same ROI, as shown in Fig. 10(a), to compare the clutter level suppression. In Fig. 11(a), POAA using 32 transmissions has a clutter level of -45.8 dB, which indicates an additional 5.8 dB of clutter suppression than conventional CPWC [-40 dB, as shown in Fig. 10(a)]. In Fig. 11(b) and (c), POAA using 96 transmissions and 128 transmissions had a clutter level of -46 and -46.5 dB, respectively. From both the quantitative measurements and visual inspections of the B-mode images of the artery, POAA was still effective at suppressing clutters included by axial lobes with incomplete transmissions. Compared with HD-SA with incomplete transmissions [see Fig. 11(d)–(f)], POAA is less susceptible to potential decoding errors and shows persistent improvement clutter rejection inside the vessel lumen [see Fig. 11(a)–(c)].

IV. Discussion

This article presents a pixel-oriented adaptive apodization technique based on the recovery of the complete dataset. The proposed method concentrates on reducing the clutters resulting from axial lobes that are commonly associated with CPWC. Through the analysis of axial lobe generation, it was demonstrated that axial lobes are caused by the spherical waves emitted from elements that are far away from the targeted location. Therefore, to suppress the axial lobe, one can implement a transmit apodization to suppress the contribution of elements that are distant from the targeted location. As shown in (13) and (14), the optimized apodization profile for every location is unique. Therefore, it is necessary to design adaptive apodization functions for each pixel location in order to suppress axial lobes throughout the entire FOV, which is extremely expensive in practice. Therefore, we proposed to use the complete dataset generated by synthetic aperture imaging to realize POAA. To address the issue of low SNR with conventional synthetic aperture imaging, we deployed Hadamard encoding and delay encoding in this study to achieve robust POAA across the entire FOV. We showed significantly improved imaging quality by using POAA in the simulation study, the phantom experiments, and the carotid artery images of a healthy volunteer.

In the phantom experiment, it can be noticed that the CNR of CPWC combined with POAA using complete transmission has an approximately 20% increase compared with CPWC alone, which is not as substantial as the improvement in the simulation study. One reason for the discrepancy in performance is the clutter signal below the upper boundary of the cyst, as shown in Fig. 8. These clutters are caused by out-of-plane signals from the boundary of the cyst in the elevational direction—the beam thickness in the elevational direction is not negligible and, therefore, casts echo from out of the plane into the FOV. POAA is not capable of suppressing out-of-plane clutters of this nature, which led to a decrease in clutter suppression performance compared to the simulation study.

POAA reduces axial lobes by limiting the transmit signal (i.e., transmit apodization) from elements that do not significantly contribute to the main lobe. It is challenging to complete this task on receive signals with unapodized transmissions because the echoes of a target from the late-arriving spherical waves (i.e., the axial lobes) are mixed with "real" echoes of the target from a deeper range. Thus, we set up an error threshold ε to control the active transmit elements that contribute to the main lobe, as denoted by (7). In practice, the error threshold ε should be carefully selected to balance the tradeoff between lateral resolution and the effectiveness of POAA: a larger ε decreases the clutter suppression performance of POAA while delivering better lateral spatial resolution with narrower main lobe width, and a smaller ε has the opposite effect. In addition, the value of ε also determines how many axial lobes will be blended into the main lobes. In the wire target simulation study, we applied a quarter length of the transmit impulse duration as ε (i.e., the transmit signal included two cycles of a modulated sinusoidal wave, and ε was set as the time length of half cycle), which is a strict limitation that excludes almost the entire length of the axial lobes and minimizes the influence from other factors (e.g., element directivity). In Fig. 5(b) and (c), POAA maintains almost the same main lobe width as conventional CPWC while delivering a 120-dB suppression of axial lobes. Therefore, the same criterion of ε was applied for *in vitro* and *in vivo* experiments using the Verasonics Vantage 256 System. The transmit impulse lasts for two cycles (i.e., 384 ns with a 5.2-MHz center frequency), and ε was selected to be a quarter cycle (i.e., 96 ns).

Conventional Hadamard encoding and delay encoding with complete transmission require the same number of transmissions as the number of transmit elements. In this article, implementing CPWC with POAA using conventional Hadamard encoding and delay encoding necessitates 192 transmissions with a 192-element transducer, which heavily restricts the frame rate and compromises the advantage of CPWC. In order to reduce the transmission number and improve the frame rate, the incomplete transmission method was proposed to

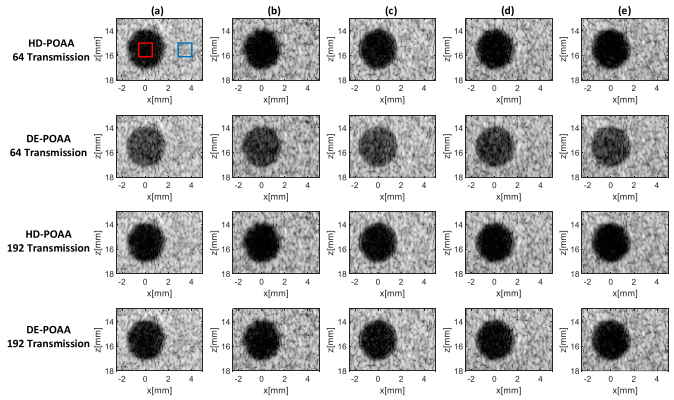

Fig. 12. Five different simulated anechoic cysts imaged using HD-POAA and DE-POAA with complete and incomplete transmissions. All images are displayed using a 50-dB dynamic range. The red and blue rectangles in (a) denote the ROI used for measuring the CNR. The red rectangle encloses the region inside the cyst, while the blue rectangle encloses the region outside the cyst. (a) Phantom 1. (b) Phantom 2. (c) Phantom 3. (d) Phantom 4. (e) Phantom 5.

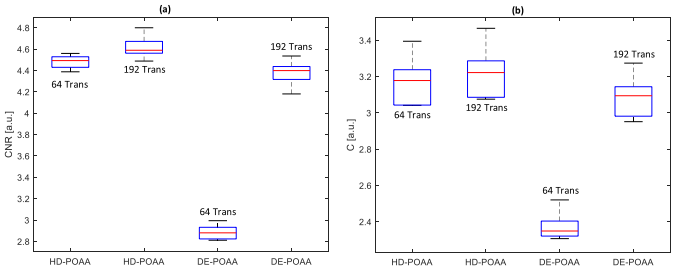

Fig. 13. (a) CNR and (b) contrast measurement of the simulated anechoic cysts in Fig. 12.

recover the complete dataset using transmissions less than the number of elements. Equations (18) and (25) give the solutions of Hadamard decoding and delay decoding using the incomplete transmission. Fig. 11 demonstrates that we can achieve a level of clutter suppression in an artery using fewer than 192 transmissions for a 192-element transducer that is comparable to the suppression achieved with a complete number of transmissions. Compared with Fig. 10(a), POAAs with three sets of incomplete transmissions all showed significant contrast improvement in the artery region over conventional CPWC. Therefore, for hypoechoic regions, such as blood vessels, it is possible to use as few as 32 transmissions for a 192-element transducer. However, using fewer transmissions does lead to more computational error in Hadamard decoding and delay decoding. The pseudoinversion with less number of transmissions brings in more interference from elements further out on the array. In Fig. 11(a), we can find more artifacts in the high-contrast region above the artery, which is caused by imprecise decoding. This indicates that, for hyperechoic regions (e.g., muscle), more transmissions (e.g., 96 or 128 transmissions for a 192-element transducer) may be necessary to provide effective axial lobe suppression. In addition, as shown in Figs. 12 and 13, the performance of the random delay encoding with incomplete transmissions also decreases compared with complete transmissions.

One limitation of POAA compared with conventional CPWC is the computational cost. Since POAA varies with pixel locations and compounding angles, the synthetization and beamforming procedure needs to repeat for reconstructing pixels of different positions or with different compounding angles. While the number of pixels is dependent on the ROI size, it is possible to choose an appropriate number of compounding angles to reduce the computing time. As shown in the simulation study in Fig. 7, the gain in CNR and CR using POAA over CPWC becomes less with an increased number of steering angles (50% at 32 angles versus 36% at 192 angles). Therefore, for the rest of the experiment in this article, we used 32 compounding angles (range from $-15°$ to $15°$ with a step size of $1°$) to balance the computational cost and the contrast improvement. For synthetization with 32 compounding angles, reconstructing one image with 100×100 pixels needs to compute DAS beamforming for $32 \times 100 \times 100 = 320\,000$ times in theory. In practice, the computing time can be reduced a lot since some of the pixels share the same apodization profile and need to be computed only once. It was tested in the simulations that reconstructing a 100×100 image needs to repeat DAS beamforming around 2000 times. Fortunately, this procedure is highly parallelizable since, for every pixel, POAA is independent and can be computed synchronously. The use of parallel computing platforms (e.g., GPU servers) will considerably improve the computation speed.

V. Conclusion

This article presents a pixel-oriented adaptive apodization aimed at the removal of the axial lobes generated in CPWC imaging. The design of the proposed apodization is based on the analysis of CPWC signals that cause axial lobes. To facilitate the practical use of POAA, two encoding techniques, including Hadamard encoding and delay encoding using random delays, were introduced for the recovery of the complete dataset. In both simulation and experiments, POAA overcomes the drawback of ADTA and substantially suppresses the axial lobe level in the entire FOV. This technique can improve the quality of CPWC imaging and has great potential for multiple imaging modalities based on CPWC.

References

[1] G. Montaldo, M. Tanter, J. Bercoff, N. Benech, and M. Fink, "Coherent plane-wave compounding for very high frame rate ultrasonography and transient elastography," *IEEE Trans. Ultrason., Ferroelectr., Freq. Control*, vol. 56, no. 3, pp. 489–506, Mar. 2009.

[2] J. Bercoff, M. Tanter, and M. Fink, "Supersonic shear imaging: A new technique for soft tissue elasticity mapping," *IEEE Trans. Ultrason., Ferroelectr., Freq. Control*, vol. 51, no. 4, pp. 396–409, Apr. 2004.

[3] C. Demené *et al.*, "Spatiotemporal clutter filtering of ultrafast ultrasound data highly increases Doppler and fultrasound sensitivity," *IEEE Trans. Med. Imag.*, vol. 34, no. 11, pp. 2271–2285, Nov. 2015.

[4] P. Song *et al.*, "Accelerated singular value-based ultrasound blood flow clutter filtering with randomized singular value decomposition and randomized spatial downsampling," *IEEE Trans. Ultrason., Ferroelectr., Freq. Control*, vol. 64, no. 4, pp. 706–716, Apr. 2017.

[5] C. Errico *et al.*, "Ultrafast ultrasound localization microscopy for deep super-resolution vascular imaging," *Nature*, vol. 527, no. 7579, pp. 499–502, Nov. 2015.

[6] L. E. Kinsler, *Fundamentals of Acoustics*, 4th ed. New York, NY, USA: Wiley, 2000.

[7] P. Y. Barthez, R. Léveillé, and P. V. Scrivani, "Side lobes and grating lobes artifacts in ultrasound imaging," *Vet. Radiol. Ultrasound*, vol. 38, no. 5, pp. 387–393, Sep. 1997.

[8] F. Dupenloup, J. Y. Chapelon, D. J. Cathignol, and O. A. Sapozhnikov, "Reduction of the grating lobes of annular arrays used in focused ultrasound surgery," *IEEE Trans. Ultrason., Ferroelectr., Freq. Control*, vol. 43, no. 6, pp. 991–998, Nov. 1996.
[9] S. Bae and T.-K. Song, "Methods for grating lobe suppression in ultrasound plane wave imaging," *Appl. Sci.*, vol. 8, no. 10, p. 1881, 2018.
[10] W. Guo, Y. Wang, and J. Yu, "A sibelobe suppressing beamformer for coherent plane wave compounding," *Appl. Sci.*, vol. 6, no. 11, p. 359, 2016.
[11] A. Rodriguez-Molares, J. Avdal, H. Torp, and L. Lovstakken, "Axial lobes in coherent plane-wave compounding," in *Proc. IEEE Int. Ultrason. Symp. (IUS)*, Sep. 2016, pp. 1–4.
[12] A. Rodriguez-Molares, H. Torp, B. Denarie, and L. Løvstakken, "The angular apodization in coherent plane-wave compounding [correspondence]," *IEEE Trans. Ultrason., Ferroelectr., Freq. Control*, vol. 62, no. 11, pp. 2018–2023, Nov. 2015.
[13] R. S. Cobbold, *Foundations of Biomedical Ultrasound*. Oxford, U.K.: Oxford Univ. Press, 2006, pp. 189–195.
[14] J. A. Jensen, S. I. Nikolov, K. L. Gammelmark, and M. H. Pedersen, "Synthetic aperture ultrasound imaging," *Ultrasonics*, vol. 44, pp. e5–e15, Dec. 2006.
[15] J. A. Jensen *et al.*, "SARUS: A synthetic aperture real-time ultrasound system," *IEEE Trans. Ultrason., Ferroelectr., Freq. Control*, vol. 60, no. 9, pp. 1838–1852, Sep. 2013.
[16] M. Karaman, P.-C. Li, and M. O'Donnell, "Synthetic aperture imaging for small scale systems," *IEEE Trans. Ultrason., Ferroelectr., Freq. Control*, vol. 42, no. 3, pp. 429–442, May 1995.
[17] R. Y. Chiao, L. J. Thomas, and S. D. Silverstein, "Sparse array imaging with spatially-encoded transmits," in *Proc. IEEE Ultrason. Symp.*, Oct. 1997, pp. 1679–1682.
[18] T. Harrison, A. Sampaleanu, and R. Zemp, "S-sequence spatially-encoded synthetic aperture ultrasound imaging [correspondence]," *IEEE Trans. Ultrason., Ferroelectr., Freq. Control*, vol. 61, no. 5, pp. 886–890, Apr. 2014.
[19] T. X. Misaridis and J. A. Jensen, "Space–time encoding for high frame rate ultrasound imaging," *Ultrasonics*, vol. 40, nos. 1–8, pp. 593–597, May 2002.
[20] P. Gong, M. C. Kolios, and Y. Xu, "Delay-encoded transmission and image reconstruction method in synthetic transmit aperture imaging," *IEEE Trans. Ultrason., Ferroelectr., Freq. Control*, vol. 62, no. 10, pp. 1745–1756, Oct. 2015.
[21] N. Bottenus, "Recovery of the complete data set from focused transmit beams," *IEEE Trans. Ultrason., Ferroelectr., Freq. Control*, vol. 65, no. 1, pp. 30–38, Jan. 2018.
[22] J. A. Jensen and N. B. Svendsen, "Calculation of pressure fields from arbitrarily shaped, apodized, and excited ultrasound transducers," *IEEE Trans. Ultrason., Ferroelectr., Freq. Control*, vol. 39, no. 2, pp. 262–267, Mar. 1992.
[23] J. A. Jensen, "Field: A program for simulating ultrasound systems," *Med. Biol. Eng. Comput.*, vol. 4, no. 1, pp. 351–353, 1996.
[24] A. N. Tikhonov and Y. V. Arsenin, *Solutions of Ill-Posed Problems*. Washington, DC, USA: V.H. Winston, 1977.
[25] N. Bottenus, "Comparison of virtual source synthetic aperture beamforming with an element-based model," *J. Acoust. Soc. Amer.*, vol. 143, no. 5, pp. 2801–2812, 2018.

Qi You (Graduate Student Member, IEEE) received the B.S. and M.S. degrees in electronic science and engineering from Nanjing University, Nanjing, Jiangsu, China, in 2016 and 2019, respectively. He is currently pursuing the Ph.D. degree with the Department of Bioengineering, University of Illinois at Urbana–Champaign, Urbana, IL, USA.

His current research interests are ultrasound beamforming and super-resolution techniques.

Zhijie Dong (Graduate Student Member, IEEE) received the B.Eng. degree in information engineering from Southeast University, Nanjing, China, in 2017, and the M.S. degree in electrical and computer engineering from the University of Michigan, Ann Arbor, MI, USA, in 2018. He is currently pursuing the Ph.D. degree with the Department of Electrical and Computer Engineering, University of Illinois at Urbana–Champaign, Urbana, IL, USA.

His current research interests are ultrafast 3-D imaging and signal processing.

Matthew R. Lowerison received the Ph.D. degree in medical biophysics from the University of Western Ontario, London, ON, Canada, in 2017.

He is currently with the Department of Electrical and Computer Engineering and the Beckman Institute for Advanced Science and Technology, University of Illinois at Urbana–Champaign, Urbana, IL, USA. His current research interests include ultrasound microvessel imaging, super-resolution ultrasound localization microscopy, and ultrasonic characterization of tumor microenvironments.

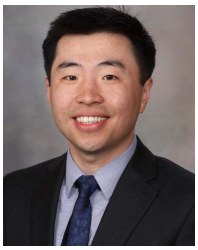

Pengfei Song (Senior Member, IEEE) received the B.S. degree in biomedical engineering from the Huazhong University of Science and Technology, Wuhan, China, in 2008, the M.S. degree in biological systems engineering from the University of Nebraska–Lincoln, Lincoln, NE, USA, in 2010, and the Ph.D. degree in biomedical engineering from the Mayo Clinic College of Medicine, Rochester, MN, USA, in 2014.

He is currently an Assistant Professor with the Department of Electrical and Computer Engineering, the Beckman Institute for Advanced Science and Technology, the Department of Bioengineering, and the Carle Illinois College of Medicine, University of Illinois at Urbana–Champaign, Urbana, IL, USA. His research interests include super-resolution ultrasound imaging, ultrafast ultrasound, deep learning, 3-D ultrafast imaging, functional ultrasound, and ultrasound shear wave elastography.

Dr. Song is also a fellow of the American Institute of Ultrasound in Medicine, a Senior Member of the National Academy of Inventors, and a Full Member of the Acoustical Society of America.